Journal of
Materials Chemistry A

PAPER

View Article Online
View Journal | View Issue

Enhanced photocatalytic mechanism for the hybrid $g\text{-}C_3N_4/MoS_2$ nanocomposite†

Cite this: *J. Mater. Chem. A*, 2014, **2**, 7960

Jiajun Wang,[a] Zhaoyong Guan,[a] Jing Huang,[ab] Qunxiang Li*[a] and Jinlong Yang[ac]

Received 17th January 2014
Accepted 28th February 2014

DOI: 10.1039/c4ta00275j

www.rsc.org/MaterialsA

Here, we explore the enhanced photocatalytic mechanism for the hybrid $g\text{-}C_3N_4/MoS_2$ nanocomposites for the first time by performing extensive density functional theory calculations. The calculated band alignment between the $g\text{-}C_3N_4$ monolayer and MoS_2 sheets clearly reveals that the conduction band minimum and valence band maximum of the $g\text{-}C_3N_4$ monolayer are higher by about 0.83 eV and 0.15 eV respectively than those of the MoS_2 sheet. This predicted type-II band alignment ensures the photogenerated electrons easily migrate from the $g\text{-}C_3N_4$ monolayer to the MoS_2 sheet, and leads to the high hydrogen-evolution reaction activity. The charge transfer between MoS_2 and $g\text{-}C_3N_4$ results in a polarized field within the interface region, which will benefit the separation of photogenerated carriers. The calculated optical absorption curves verify that this proposed layered nanocomposite is a good light-harvesting semiconductor. Moreover, a $g\text{-}C_3N_4$ bilayer covering a MoS_2 sheet also displays desirable properties. These findings indicate that the MoS_2 sheet is a promising candidate as a non-noble metal co-catalyst for $g\text{-}C_3N_4$ photocatalysts, and also provide useful information for understanding the observed enhanced photocatalytic mechanism in experiments.

Introduction

The production of chemical fuels by solar energy conversion is an attractive and sustainable solution to the depletion of fossil fuels and serious environmental problems. H_2 will play an important role in this field because it is an ultimate clean energy and can be used in fuel cells.[1–3] Due to the pioneering work of Fujishima and Honda,[4] who demonstrated that overall water splitting can be achieved using a photoelectrochemical cell consisting of a single-crystalline TiO_2 anode and a Pt cathode under ultraviolet (UV) irradiation and an external bias, photocatalytic water splitting has been intensively investigated in the past four decades, as a promising strategy for clean, low-cost, and environmentally friendly production of H_2 by utilizing solar energy.[5–12] At present, most photocatalysts are metal oxides, sulfides and nitrides with d^0 or d^{10} transition metal cations.[13] Unfortunately, most of these catalysts are active only under UV irradiation, while others absorbing visible light are not stable during the reaction process: for example photocorrosion occurs in CdS.[6] Photocatalysts for practical use with relatively high productivity have not yet been found. Searching for new efficient photocatalysts both from theoretical and experimental viewpoints is urgently needed.

Metal-free photocatalysts may have the advantages of non-toxicity and good processability, and are gradually becoming important catalysts. The recently discovered graphitic carbon nitrides ($g\text{-}C_3N_4$), with a band gap of about 2.7 eV to absorb blue light, have attracted increasing attention for photocatalytic water splitting.[14–19] $g\text{-}C_3N_4$ was found not only to be a chemically and thermally stable semiconductor, but also to be capable of achieving both half reactions of water splitting under visible light, meaning that the band-gap covers both the water reduction and water oxidation potentials.[14] However, like many other photocatalysts, the photocatalytic H_2 production activity of pristine $g\text{-}C_3N_4$ remains poor, and it strongly relies on the type and amount of surface co-catalysts.[20,21] The co-catalyst can provide reduction or oxidation active sites, catalyze the surface reactions by lowering the activation energies, trapping the charge carriers, and suppressing the recombination of photogenerated electrons and holes.[22] Thus, choosing proper co-catalysts loaded on the light harvesting semiconductor (*i.e.* $g\text{-}C_3N_4$) can lead to good photocatalytic performance, including activity, selectivity, and stability. In general, the photocatalytic performance always depends on the nature of the light harvesting semiconductor and the functions of the co-catalysts. However, the co-catalysts used are mainly noble metals (*i.e.* Pt) or their oxides, which are scarce and expensive.[23] Therefore, more attention should be paid to identifying alternative co-catalysts based on non-noble metals.

---

[a] *Hefei National Laboratory for Physical Sciences at the Microscale, University of Science and Technology of China, Hefei, Anhui 230026, China. E-mail: liqun@ustc.edu.cn*

[b] *School of Materials and Chemical Engineering, Anhui Jianzhou University, Hefei, Anhui 230022, China*

[c] *Synergetic Innovation Center of Quantum Information and Quantum Physics, University of Science and Technology of China, Hefei, Anhui 230026, China*

† Electronic supplementary information (ESI) available: The calculated band structures with different exchange mixing parameters, the DOS, PDOS and band alignment at the PBE level, INCAR and POSCAR files. See DOI: 10.1039/c4ta00275j

During the past few years, owing to its high hydrogen-evolution reaction (HER) activity as an electrocatalyst, layered molybdenum disulfide (MoS_2) has been extensively investigated as a promising electrocatalyst for H_2 evolution and has been considered as a promising alternative for Pt due to its high abundance and low cost.[24–31] To date, MoS_2 sheets as a co-catalyst for photocatalytic H_2 production have received a lot of experimental attention. For instance, Zong *et al.*[32] have shown that the photocatalytic H_2 production activity of CdS could be enhanced by loading with MoS_2 sheets. Xiang *et al.*[33] have reported that Ti-based composite photocatalysts containing a layered MoS_2/graphene co-catalyst afford an effective photocatalyst for H_2 production. Such enhanced photocatalytic performance has been ascribed to the synergistic effects caused by the interfacial interaction between the MoS_2 sheets and the photocatalyst. Most recently, Hou *et al.*[34] have designed earth-abundant organic–inorganic layered heterojunctions by gas-controlled growth of thin layered MoS_2 on a mesoporous g-C_3N_4 surface. These hybrid junctions exhibited enhanced photocatalytic hydrogen evolution activity under visible-light irradiation, and their performance was comparable to that of Pt/g-C_3N_4 under their reaction conditions. According to these experimental results, it seems that MoS_2 sheets can serve as suitable co-catalysts to composite with light harvesting semiconductors, and show enhanced photocatalytic performance. However, the atomic details at the interface between the MoS_2 sheets and the light harvesting semiconductor remain poorly understood. In addition, there is still a lack of fundamental understanding of the effects of interfacial composition and the mechanisms behind such photocatalytic enhancement of light harvesting semiconductors modified with MoS_2.

Here, we perform extensive density functional (DFT) calculations to characterize the interface between g-C_3N_4 and MoS_2 sheets, and then to clarify the underlying mechanism of enhancement of the photocatalytic performance. We find that there is some charge transfer from g-C_3N_4 to MoS_2, forming a polarized field around the interface region. This leads to enhanced photocatalytic efficiency through reducing e^-–h^+ pair recombination. Moreover, our calculations clearly reveal that nearly perfect band alignment exists between g-C_3N_4 (both mono- and bilayer) and MoS_2 sheets. The photogenerated electrons can easily migrate from g-C_3N_4 layer(s) to MoS_2 sheets, which ensures the high HER activity. Moreover, the theoretical findings obtained in this work can be used to understand the experimental results, which can also be extended for future studies of other layered junctions.

Computational details

Our DFT calculations are performed by using the Vienna *ab initio* simulation package (VASP).[35,36] The interaction between the core and valence electrons is described using the frozen-core projector augmented wave approach.[37] To optimize their geometric structures, the generalized gradient approximation of Perdew–Burke–Ernzerhof (PBE) form[38] with van der Waals (vdW) correction proposed by Grimme[39,40] is chosen due to its good description of long-range vdW interactions.[41,42] The energy cutoff is set to be 520 eV. A Monkhorst–Pack mesh of[43] $2 \times 2 \times 1$ and $6 \times 6 \times 1$ k-points is used to sample the two-dimensional Brillouin zone for geometry optimizations and electronic structure calculations, respectively. The vacuum space is set to be at least 15 Å to separate the interactions between neighboring slabs. All geometry structures are fully relaxed until the convergence criteria of energy and force are less than 10^{-5} eV and 0.01 eV $Å^{-1}$, respectively.

The band alignment between g-C_3N_4 and layer MoS_2 sheet is one central issue of this study. Considering that in general the PBE functional underestimates the band gaps of semiconductors,[44] all electronic structures are calculated using the Heyd–Scuseria–Ernzerhof (HSE06) hybrid functional.[45] In the default HSE06 functional, the full PBE correlation energy is added, and 1/4 of the PBE exchange is replaced by the Hartree–Fock exact exchange. Namely, the Hartree–Fock exchange mixing parameter (a) in the HSE06 functional is set to be 0.25. Unfortunately, the band gaps of g-C_3N_4 and MoS_2 sheets are predicted to be 3.19 and 2.14 eV respectively by using the HSE06 functional with $a = 0.25$ (as shown in Fig. S1 in ESI†), which are seriously overestimated.[18,47,48] In order to reproduce the experimental band gaps of isolated g-C_3N_4 and MoS_2 sheets, the value of a is decreased from 0.25 to 0.175 in the present work.

To explore the optical properties of g-C_3N_4/MoS_2 nanocomposites, the optical absorption spectra are simulated by converting the complex dielectric function to the absorption coefficient α_{abs} according to the following relation,[46]

$$\alpha_{abs} = \sqrt{2}\omega\left(\sqrt{\varepsilon_1{}^2(\omega) + \varepsilon_2{}^2(\omega)} - \varepsilon_1(\varepsilon)\right)^{\frac{1}{2}}$$

where $\varepsilon_1(\omega)$ and $\varepsilon_2(\omega)$ are the real and imaginary parts, respectively, of the frequency dependent complex dielectric function $\varepsilon(\omega)$. Taking into account the tensor nature of the dielectric function, $\varepsilon_1(\omega)$ and $\varepsilon_2(\omega)$ are averaged over three polarization vectors (along x, y, and z directions).

Results and discussion

Before investigating g-C_3N_4/MoS_2 nanocomposite, we firstly examine the isolated g-C_3N_4 and MoS_2 sheets. In our calculations, the lattice constants of free MoS_2 and g-C_3N_4 are predicted to be 3.19 and 4.79 Å, respectively, which agree well with previous experimental measurements and theoretical results.[18,47,48] For a g-C_3N_4 monolayer, due to the different chemical environments, N atoms are divided into two kinds (N1 and N2), where N1 atoms are fully saturated by the surrounding C atoms, while N2 atoms only connect two C atoms, leaving a non-bonding character, while all C atoms have three nearest-neighbor N atoms, as shown in Fig. 1(a). The C–N1 and C–N2 distances are 1.47 and 1.33 Å, respectively. The calculated band structure and density of states (DOS) of g-C_3N_4 monolayer are plotted in Fig. 1(b) and (c), respectively. Clearly, a g-C_3N_4 sheet is a semiconductor with a direct energy gap of 2.7 eV. The electrons of N1 and C atoms only occupy the states far away from the valence band maximum (VBM), and the VBM is dominated by the N2 atoms. The calculated partial DOS (PDOS)

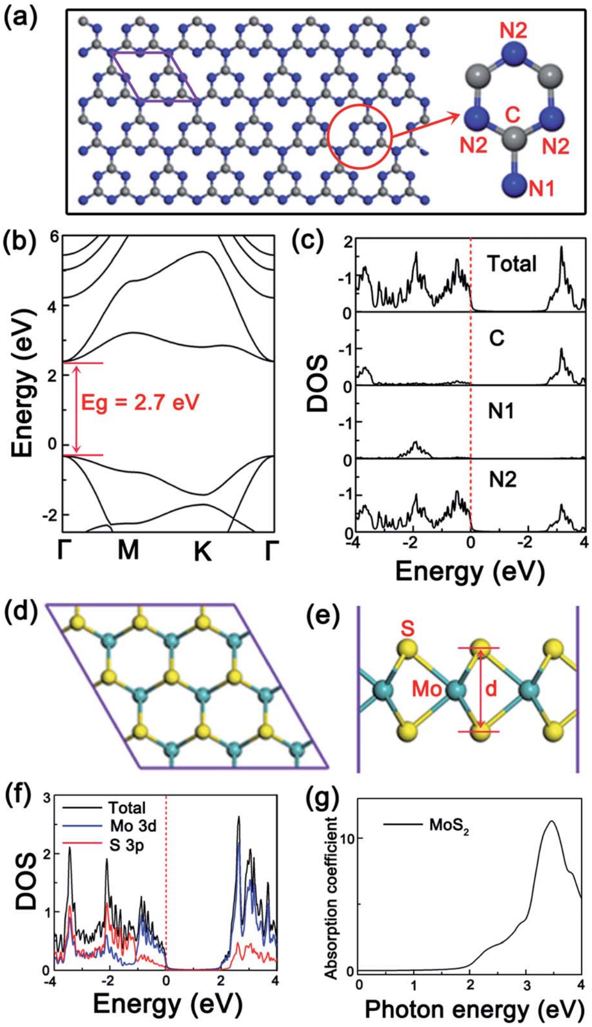

Fig. 1 (a) g-C_3N_4 monolayer. Here, the purple lines show the unit cell in our calculations; the gray and blue balls stand for C and N atoms, respectively. (b) The corresponding calculated band structure and (c) PDOS of g-C_3N_4 monolayer. (d) Top and (e) side views of a MoS_2 sheet. Here, the green and yellow balls stand for Mo and S atoms, respectively. (f) The corresponding calculated PDOS, and (g) absorption coefficients of MoS_2 sheets.

well reflects the different chemical bonding environments. These observations are similar to the previous reports.[18]

The top and side views of an optimized MoS_2 sheet with a honeycomb structure analogous to graphene are illustrated in Fig. 1(d) and (e), and its DOS and absorption coefficients are presented in Fig. 1(f) and (g), respectively. We find that the ground state of the MoS_2 sheet is a semiconductor with a direct band gap energy of 2.0 eV, the Mo–S bond length is 2.42 Å and the vertical S–S distance (d) is 3.13 Å. These results are consistent with the previous works.[49–52] By analyzing the PDOS of the MoS_2 sheet, we can see that the electronic states near the conduction band minimum (CBM) and VBM are all mainly contributed by Mo 4d orbitals and the S 3p orbitals. Moreover, there is a strong hybridization between the Mo 4d orbitals and the S 3p orbitals, which leads to a large splitting between the bonding and antibonding states. As shown in Fig. 1(g), the optical absorption of MoS_2 sheets increases significantly with photon energy over the range of visible light and reaches a maximum absorption at 3.4 eV, which agrees well with previous results.[53] This absorption peak arises from the optical transition between the valence band (VB) and conduction band (CB) around the K point. It should be pointed out that MoS_2 sheets seem to have a suitable band gap with visible light response, however, it is not an excellent material for water splitting due to photocorrosion, which always is a demerit point of metal sulfide materials.[6]

To understand the enhanced photocatalytic activity of the g-C_3N_4/MoS_2 nanocomposite under visible light irradiation observed in experiments,[34] we propose a g-C_3N_4/MoS_2 nanocomposite model in which a 3 × 3 supercell of MoS_2 sheet is used to match a 2 × 2 cell of g-C_3N_4 monolayer, and the lattice mismatch is less than 1.0%. The top and side views of the g-C_3N_4/MoS_2 nanocomposite are shown in Fig. 2(a) and (b), respectively. Due to the presence of the MoS_2 sheet, g-C_3N_4 displays obvious geometric distortion, as shown in Fig. 2(b). The corresponding buckling distance (h1) is about 0.92 Å. The vertical separation (h2) between MoS_2 sheet and g-C_3N_4 monolayer is predicted to be 2.97 Å, which is a typical vdW equilibrium spacing. These results are consistent with the previous results.[54,55] To address the interaction between the g-C_3N_4 monolayer and MoS_2 sheets, we calculate the interface adhesion energy, which is defined as $E_b = E_{g\text{-}C_3N_4/MoS_2} - E_{MoS_2} - E_{g\text{-}C_3N_4}$; here, $E_{g\text{-}C_3N_4/MoS_2}$, E_{MoS_2}, and $E_{g\text{-}C_3N_4}$ are the total energies of the relaxed g-C_3N_4/MoS_2 nanocomposite, MoS_2, and g-C_3N_4 layers, respectively. The negative E_b denotes that the interface structure between MoS_2 and g-C_3N_4 layers is stable. The E_b is predicted to be −1.41 eV for the examined g-C_3N_4/MoS_2 nanocomposite, which is comparable with recent theoretical predictions in other g-C_3N_4-based nanocomposites, such as graphene/g-C_3N_4 and g-C_3N_4/$ZnWO_4$ systems,[54,56] indicating that the g-C_3N_4 monolayer strongly interacts with MoS_2 sheets, and the corresponding nanocomposite is stable.

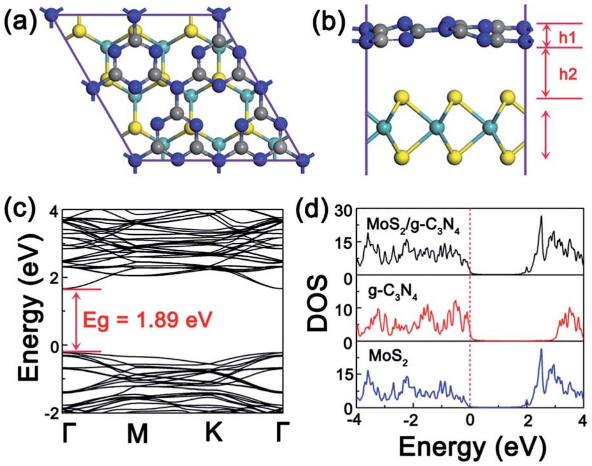

Fig. 2 (a) The top view of the proposed g-C_3N_4/MoS_2 nanocomposite, and (b) the side view. (c) The calculated band structure, (d) TDOS and PDOS of g-C_3N_4/MoS_2 nanocomposite. Here, the red and blue lines stand for the PDOS of g-C_3N_4 monolayer and MoS_2 sheet, respectively. The Fermi level is set to zero for clarity.

To describe the g-C_3N_4-MoS_2 interaction more clearly, it is insightful to analyse their electronic structures. The band structure and total DOS of g-C_3N_4/MoS_2 nanocomposite as well as the PDOS of MoS_2 and g-C_3N_4 monolayers are plotted in Fig. 2(c) and (d), respectively. Comparing with the band gaps of g-C_3N_4 (2.7 eV) and MoS_2 sheets (2.0 eV), the band gap of the g-C_3N_4/MoS_2 nanocomposite is reduced to about 1.89 eV due to the g-C_3N_4–MoS_2 interaction. This implies that the electron transfer from VB to CB in the g-C_3N_4/MoS_2 nanocomposite becomes more easy. Consequently, this results in the red shift of the optical absorption edge.

As shown in Fig. 2(d), the main shape of the calculated DOS projected on two different layers in the proposed hybrid nanocomposite is similar to that of the TDOS of isolated MoS_2 and the g-C_3N_4 monolayers, as shown in Fig. 1(c) and (e), respectively. This is easy to understand, since the separation between MoS_2 and g-C_3N_4 layers (2.97 Å) is relatively large, which indicates that the g-C_3N_4–MoS_2 interaction is not very strong due to the absence of covalent bonding upon formation of this hybrid interface. We find that the intrinsic band gap of the g-C_3N_4 monolayer in the nanocomposite (2.68 eV) has a tiny change, compared with that of the isolated g-C_3N_4 layer (2.70 eV). This implies that the electron transfer from N 2p at the VB to C 2p and N 2p at the CB is the dominant process, which excludes the band gap narrowing effect of g-C_3N_4 on improving the hydrogen-production performance.

Moreover, Fig. 2(d) clearly indicates that the band gap of g-C_3N_4 in the nanocomposite spans from 0.0 to 2.68 eV, and MoS_2 has a 2.0 eV band gap spanning from −0.15 to 1.85 eV. The top part of the VB is mainly contributed by g-C_3N_4, while the states from the MoS_2 sheet are located at a relatively low position (0.15 eV). This indicates that the valence band offset (VBO) between g-C_3N_4 and MoS_2 is about 0.15 eV. On the other hand, the bottom part of the CB mainly comes from the states of MoS_2 sheets, while the position of the states from g-C_3N_4 are high, about 0.83 eV, which means that the conduction band offset (CBO) between g-C_3N_4 and MoS_2 is about 0.83 eV. These observations imply that once the g-C_3N_4 monolayer covers the MoS_2 sheet, the band alignment between the two layered materials results in the formation of a type-II heterojunction.[57,58] This is the first key finding to understand the enhanced photoactivity of the proposed g-C_3N_4/MoS_2 nanocomposite, which will be discussed in more detail below. Note that this finding is not sensitive to the adopted functional in DFT calculations. Both PBE and HSE06 functional calculations show type-II band alignment, although the absolute values of the band gaps of MoS_2 and g-C_3N_4 monolayers depend on the used functional (Fig. S2 and S3 in ESI†).

To explore the charge transfer process in the g-C_3N_4/MoS_2 nanocomposite, the charge density differences obtained by subtracting the electronic charge of a hybrid g-C_3N_4/MoS_2 nanocomposite from that of the free MoS_2 and g-C_3N_4 monolayers are calculated and shown in Fig. 3. Here, the red and blue colors represent charge accumulation and depletion, respectively. It is clear that the charge redistribution mainly occurs at the interface region. Although the large separation between the g-C_3N_4 and MoS_2 sheet leads to the weak donor–acceptor coupling, there is some charge transfer from the g-C_3N_4 to the MoS_2 sheet. That is to say, the holes accumulate in the g-C_3N_4 region, while the electrons accumulate in the region close to the MoS_2 sheet. Therefore, in the junction region a polarized field is generated which points from g-C_3N_4 to the MoS_2 sheet. This is the second key finding which can prevent the recombination of photogenerated electrons and holes. Moreover, with help of this nice separation of e^-–h^+ pairs, the lifetime of photoinduced carriers is effectively prolonged, which is beneficial for photocatalysis. In this sense, the MoS_2 sheet shows a positive effect on the photocatalytic performance of the g-C_3N_4/MoS_2 nanocomposite.

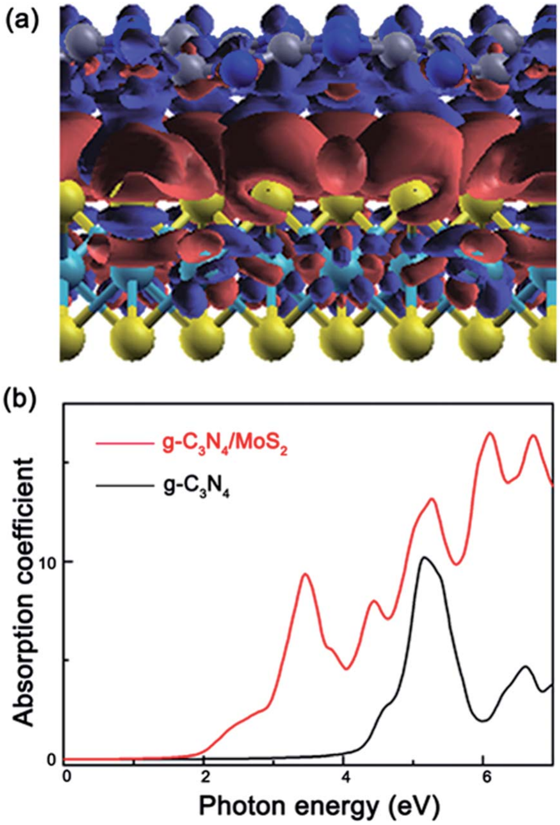

Fig. 3 (a) Charge density differences in the g-C_3N_4/MoS_2 nanocomposite. The red and blue regions represent charge accumulation and depletion, respectively, and the isosurface value is 0.001 e $Å^{-3}$. (b) The calculated absorption coefficients of the g-C_3N_4 monolayer and the g-C_3N_4/MoS_2 nanocomposite, which are labeled with the black and red lines, respectively.

To examine the combination effect of g-C_3N_4 sheet and MoS_2 sheet, the optical absorption curves of the g-C_3N_4 monolayer and the hybrid g-C_3N_4/MoS_2 nanocomposite are calculated and plotted in Fig. 3(b) with black and red lines, respectively. In general, the optical absorption behavior of a semiconductor photocatalyst, a key factor in determining its photocatalytic activity, is strongly related to its electronic structure.[59] As shown in Fig. 3(c), g-C_3N_4 monolayer has a moderate direct energy gap (2.7 eV), which means it should be a suitable visible-light absorber. However, we find that the g-C_3N_4 monolayer has absorption above 4.0 eV, which is significantly larger than the direct energy gap at the Γ point. A similar phenomenon has been observed by Wu *et al.*[60] They suggested that the orbital overlap and the optical transitions between CBM and VBM are negligible, leading to light absorption in a high energy region. One can expect that the g-C_3N_4/MoS_2 nanocomposite should display improved optical properties when the g-C_3N_4 layer covers the MoS_2 sheet. This is verified by the calculated optical adsorption curve of the g-C_3N_4/MoS_2 nanocomposite, as shown in Fig. 3(b). Clearly, compared with the g-C_3N_4 monolayer, the proposed hybrid nanocomposite exhibits more effective UV absorption and enhanced low-energy visible light response. The red shift of the absorption edge is as large as 2.0 eV for the g-C_3N_4/MoS_2 nanocomposite because electrons can be directly excited from the VB of the g-C_3N_4 layer to the CB of the MoS_2 sheet.

From the above presented DOSs of the proposed MoS_2/g-C_3N_4 nanocomposite, the band alignment is illustrated in Fig. 4. Clearly, the g-C_3N_4/MoS_2 nanocomposite is a type-II heterojunction.[57,58] The CB and VB of g-C_3N_4 monolayers are more positive than the corresponding bands of the MoS_2 sheet. Thus, when this proposed nanocomposite is illuminated with light, the electrons can be photo-excited from the CBs of both MoS_2 and g-C_3N_4 monolayers. Note that these photogenerated electrons in the g-C_3N_4 layer can be easily moved to the CB of the MoS_2 sheet due to the observed CBO. Since the MoS_2 sheet has sufficient chemical potential for the electrons to react with protons to produce hydrogen at HER active sites,[24–31] these photogenerated electrons can be effectively utilized. On the other hand, the VBM offset between the two layered materials provides the redistribution of electrons and holes, as shown in Fig. 3(a). That is to say, the oxidation and redox reactions could take place in g-C_3N_4 and MoS_2 sheets, respectively. At the same time, the energy-wasteful e^-–h^+ recombination could be greatly reduced.

It should be pointed out that the polarized field between g-C_3N_4 and MoS_2 sheets in the nanocomposite prevents the photogenerated electrons migrating from the g-C_3N_4 monolayer to the MoS_2 sheet. Therefore, there is a competitive role in electron–hole separation between the band alignment and electric polarized field. According to the estimated values, we find that the electric field strength coming from the band alignment, as shown in Fig. 4, is about three times larger than that of the dipole-induced polarized field (see ESI†). This indicates that the migration of photogenerated electrons in the g-C_3N_4/MoS_2 nanocomposite is dominated by the strong driving force provided by the type-II band alignment.

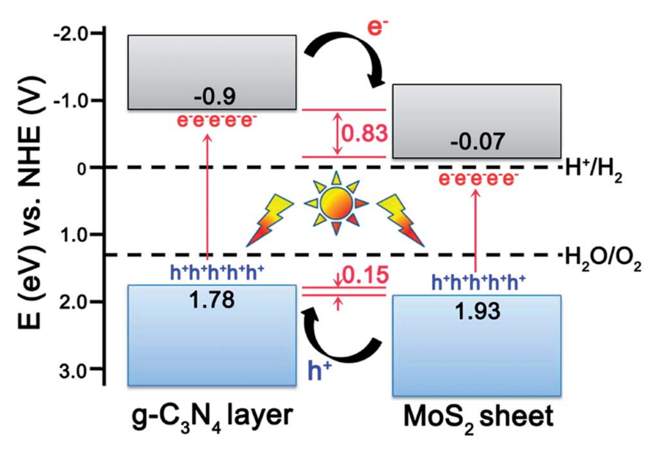

Fig. 4 Schematic illustration of the carrier transfer and separation in the proposed g-C_3N_4/MoS_2 nanocomposite.

As a typical metal sulfide photocatalyst, MoS_2 can be photocorroded under band gap excitation since the S^{2-} in MoS_2 photocatalysts rather than H_2O is oxidized by photogenerated holes.[6] As shown in Fig. 4, the photogenerated holes in the MoS_2 sheet can easily move to the g-C_3N_4 monolayer in the g-C_3N_4/MoS_2 nanocomposite due to the type-II band alignment. This may well resolve the photocorrosion problem of MoS_2 sheets in this proposed nanocomposite. These findings reveal that MoS_2 is a promising candidate as a non-noble metal co-catalyst for g-C_3N_4 photocatalysts, which can rationalize the significant enhancement of visible light photoactivity of g-C_3N_4 by growing with MoS_2 sheets.[34]

Above, we focus on the hybrid nanocomposite with a g-C_3N_4 monolayer covering the MoS_2 sheet. Actually, g-C_3N_4 synthesized in experiments is usually nanometer-scale thickness, which includes a few atomic layers.[14,18] Thus, an interesting question is whether the type-II band alignment happens or not when the number of g-C_3N_4 atomic layers increases. Firstly, we investigate the geometric and electronic structures of a g-C_3N_4 bilayer (labelled as BL-g-C_3N_4) as an example. Eight kinds of nonequivalent structures of BL-g-C_3N_4 according to the different symmetries are examined. Among them, the top and side views of the most stable structure of BL-g-C_3N_4 are shown in Fig. 5(a) and (b), respectively. The corresponding buckling distances of the top layer (*h*1) and the bottom layer (*h*3) are both about 0.70 Å, which are smaller than those of the g-C_3N_4 monolayer (0.92 Å). The vertical distance between two g-C_3N_4

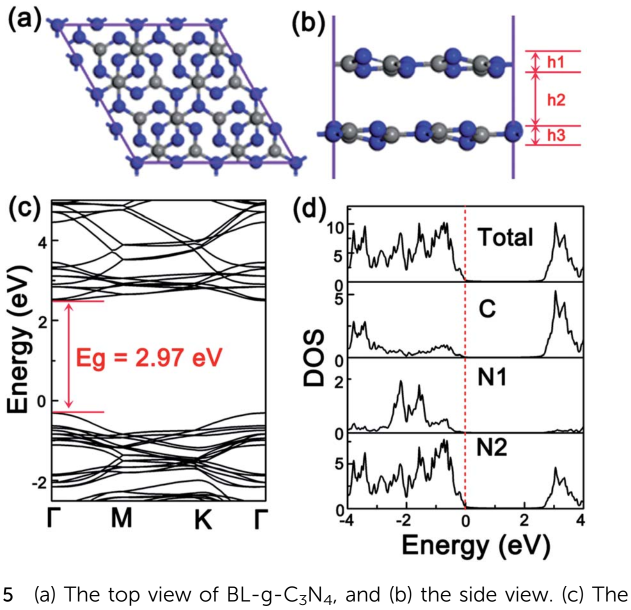

Fig. 5 (a) The top view of BL-g-C_3N_4, and (b) the side view. (c) The corresponding calculated band structure, and (d) the TDOS of BL-g-C_3N_4 and PDOS of C, N1 and N2 atoms.

layers is about 2.57 Å. The corresponding binding energy is predicted to be 0.67 eV, indicating a relatively strong chemical bonding between two g-C_3N_4 layers. This is totally different with the weak interactions in other two-dimensional bilayers, such as a graphene bilayer[61] and a graphene/BN bilayer.[62] To explore the stacking effect in the most stable g-C_3N_4 bilayer, we calculate the band structure and PDOS of a g-C_3N_4 bilayer, as shown in Fig. 5(c) and (d), respectively. It is clear that the BL-g-C_3N_4 displays semiconducting character with a direct energy gap (2.97 eV), and its band gap is enlarged by about 0.27 eV compared with the g-C_3N_4 monolayer (2.7 eV).

Then, we turn to examine BL-g-C_3N_4 loading on the MoS_2 sheet. The top and side views of this new proposed nanocomposite are illustrated in Fig. 6(a) and (b), respectively. Due to the presence of the MoS_2 sheet, BL-g-C_3N_4 displays an obvious geometric change. The corresponding buckling distances of the top layer ($h1$) and the bottom layer ($h3$) of BL-g-C_3N_4 are about 0.83 and 0.81 Å, respectively, while the distance ($h2$) between the two g-C_3N_4 layers is 2.29 Å, which is smaller than that of the g-C_3N_4 monolayer (2.57 Å). The typical vdW equilibrium space ($h4$) between BL-g-C_3N_4 and the MoS_2 sheet is about 3.16 Å, which is slightly larger than that of g-C_3N_4 monolayer loading on a MoS_2 sheet (2.97 Å), as shown in Fig. 2(a). This observation is consistent with the small interface adhesion energy (−1.37 eV) of BL-g-C_3N_4 covering a MoS_2 sheet. To analyze the carrier migration path in the interface between BL-g-C_3N_4 and the MoS_2 sheet, the TDOS and PDOS projected on individual MoS_2 and BL-g-C_3N_4 in this BL-g-C_3N_4/MoS_2 nanocomposite are presented in Fig. 6(c). Similar to the first proposed g-C_3N_4/MoS_2 nanocomposite, the band alignment of the BL-g-C_3N_4/MoS_2 nanocomposite shows that it is also a type-II heterojunction. It is clear that the CB (VB) edge of BL-g-C_3N_4 is higher than the CB (VB) edge of the MoS_2 sheet. There is a band gap of about 1.98 eV between the VB edge of BL-g-C_3N_4 and the CB edge of the MoS_2 sheet. The obtained band structures provide the possibility of the directional migration of photogenerated electrons from BL-g-C_3N_4 to the MoS_2 sheet, and this offers sufficient chemical potential for the photogenerated electrons to react with protons to produce hydrogen at HER active sites of the MoS_2 sheet.[24–31]

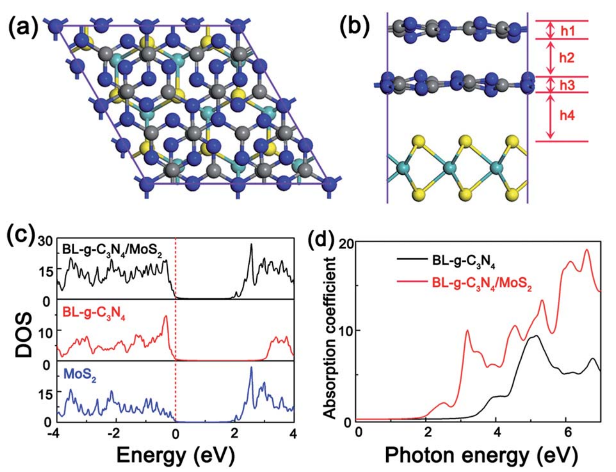

Fig. 6 (a) The top view of BL-g-C_3N_4/MoS_2 nanocomposite, (b) the side view, and (c) the corresponding TDOS of the BL-g-C_3N_4/MoS_2 nanocomposite, and the PDOS of BL-g-C_3N_4/MoS_2 and the MoS_2 sheet are plotted with black, red and blue lines, respectively. The Fermi level is set to zero for clarity. (d) The optical adsorption spectra of BL-g-C_3N_4 and theBL-g-C_3N_4/MoS_2 nanocomposite, labeled with black and red lines, respectively.

Finally, we calculate the absorption spectra of BL-g-C_3N_4 and the BL-g-C_3N_4/MoS_2 nanocomposite and plot them in Fig. 6(d). Comparing to g-C_3N_4 monolayer loading on the MoS_2 sheet, we find that the covered BL-g-C_3N_4 has much better optical absorption below 3.0 eV. This agrees well with the previous results,[60] which reported that the interlayer coupling modifies the orbitals, leading to stronger overlap of CBM and VBM of BL-g-C_3N_4. Thus, it improves the visible-light absorption. As seen in Fig. 6(d), this examined BL-g-C_3N_4/MoS_2 nanocomposite indeed displays expanded optical absorption from UV into visible light, therefore it can efficiently harvest a broad range of visible light.

Conclusions

In summary, we performed extensive DFT calculations to explore the enhanced photocatalytic mechanism for the hybrid MoS_2/g-C_3N_4 nanocomposites, including both g-C_3N_4 mono- and bilayer loading on MoS_2 sheets. The calculated band alignment between the g-C_3N_4 monolayer and the MoS_2 sheet reveals that the CBM (VBM) of g-C_3N_4 is higher by about 0.83 eV (0.15 eV) than that of the CBM (VBM) of the MoS_2 sheet. This predicted type-II band alignment ensures the photogenerated electrons can easily migrate from the g-C_3N_4 layer to the MoS_2 sheet, and leads to high HER activity. The charge transfer between MoS_2 and g-C_3N_4 results in a polarized field within the interface region, which can effectively improve the separation efficiency of these photogenerated carriers. In addition, this hybrid layered junction has high light absorption ability. Similar results are also obtained for a g-C_3N_4 bilayer covering a MoS_2 sheet. These theoretical predictions provide insight to understand the related experimental observations, and verify that MoS_2 sheets are a promising candidate as a non-noble metal co-catalyst for g-C_3N_4 photocatalysts.

Acknowledgements

We thank Professor Zhenyu Zhang for helpful discussions. This work was partially supported by National Key Basic Research Program (no. 2011CB921400 and 2014CB921101), by the Strategic Priority Research Program (B) of the CAS (no. XDB01020000), by the National Natural Science Foundation of China (no. 11074235, 21273208, 21273210, 11034006), by the Fundamental Research Funds for the Central Universities, by China Postdoctoral Science Foundation (no. 2012M511409), by the USTC-HP HPC project, and by the SCCAS and Shanghai Supercomputer Center.

Notes and references

1 J. A. Turner, *Science*, 1999, **285**, 687–689.

2 M. S. Dresselhaus and I. L. Thomas, *Nature*, 2001, **414**, 332–337.
3 N. S. Lewis and D. G. Nocera, *Proc. Natl. Acad. Sci. U. S. A.*, 2006, **103**, 15729–15735.
4 A. Fujishima and K. Honda, *Nature*, 1972, **238**, 37–38.
5 K. Maeda and K. Domen, *J. Phys. Chem. C*, 2007, **111**, 7851–7861.
6 A. Kudo and Y. Miseki, *Chem. Soc. Rev.*, 2009, **38**, 253–278.
7 X. Chen, S. Shen, L. Guo and S. S. Mao, *Chem. Rev.*, 2010, **110**, 6503–6570.
8 K. Maeda and K. Domen, *J. Phys. Chem. Lett.*, 2010, **1**, 2655–2661.
9 N. Serpone and A. V. Emeline, *J. Phys. Chem. Lett.*, 2012, **3**, 673–677.
10 H. Tong, S. Ouyang, Y. Bi, N. Umezawa, M. Oshikiri and J. Ye, *Adv. Mater.*, 2012, **24**, 229–251.
11 K. Maeda, *Phys. Chem. Chem. Phys.*, 2013, **15**, 10537–10548.
12 F. E. Osterloh, *Chem. Soc. Rev.*, 2013, **42**, 2294–2320.
13 Y. Inoue, *Energy Environ. Sci.*, 2009, **2**, 364–386.
14 X. Wang, K. Maeda, A. Thomas, K. Takanabe, G. Xin, J. M. Carlsson, K. Domen and M. Antonietti, *Nat. Mater.*, 2008, **8**, 76–80.
15 G. Liu, P. Niu, C. Sun, S. C. Smith, Z. Chen, G. Q. Lu and H.-M. Cheng, *J. Am. Chem. Soc.*, 2010, **132**, 11642–11648.
16 Y. Zhang, T. Mori, J. Ye and M. Antonietti, *J. Am. Chem. Soc.*, 2010, **132**, 6294–6295.
17 Y. Wang, J. Zhang, X. Wang, M. Antonietti and H. Li, *Angew. Chem., Int. Ed.*, 2010, **49**, 3356–3359.
18 G. Dong, K. Zhao and L. Zhang, *Chem. Commun.*, 2012, **48**, 6178–6180.
19 J. Zhang, M. Zhang, R.-Q. Sun and X. Wang, *Angew. Chem., Int. Ed.*, 2012, **51**, 10145–10149.
20 K. Maeda, X. Wang, Y. Nishihara, D. Lu, M. Antonietti and K. Domen, *J. Phys. Chem. C*, 2009, **113**, 4940–4947.
21 Y. Di, X. Wang, A. Thomas and M. Antonietti, *ChemCatChem*, 2010, **2**, 834–838.
22 J. Yang, D. Wang, H. Han and C. Li, *Acc. Chem. Res.*, 2013, **46**, 1900–1909.
23 P. C. K. Vesborg and T. F. Jaramillo, *RSC Adv.*, 2012, **2**, 7933–7947.
24 T. F. Jaramillo, K. P. Jorgensen, J. Bonde, J. H. Nielsen, S. Horch and I. Chorkendorff, *Science*, 2007, **317**, 100–102.
25 D. Merki and X. Hu, *Energy Environ. Sci.*, 2011, **4**, 3878–3888.
26 H. I. Karunadasa, E. Montalvo, Y. Sun, M. Majda, J. R. Long and C. J. Chang, *Science*, 2012, **335**, 698–702.
27 A. B. Laursen, S. Kegnaes, S. Dahl and I. Chorkendorff, *Energy Environ. Sci.*, 2012, **5**, 5577–5591.
28 H. Vrubel, D. Merki and X. Hu, *Energy Environ. Sci.*, 2012, **5**, 6136–6144.
29 T. Wang, L. Liu, Z. Zhu, P. Papakonstantinou, J. Hu, H. Liu and M. Li, *Energy Environ. Sci.*, 2013, **6**, 625–633.
30 Y. Li, H. Wang, L. Xie, Y. Liang, G. Hong and H. Dai, *J. Am. Chem. Soc.*, 2011, **133**, 7296–7299.
31 Z. Chen, D. Cummins, B. N. Reinecke, E. Clark, M. K. Sunkara and T. F. Jaramillo, *Nano Lett.*, 2011, **11**, 4168–4175.
32 X. Zong, H. Yan, G. Wu, G. Ma, F. Wen, L. Wang and C. Li, *J. Am. Chem. Soc.*, 2008, **130**, 7176–7177.
33 Q. Xiang, J. Yu and M. Jaroniec, *J. Am. Chem. Soc.*, 2012, **134**, 6575–6578.
34 Y. Hou, A. B. Laursen, J. Zhang, G. Zhang, Y. Zhu, X. Wang, S. Dahl and I. Chorkendorff, *Angew. Chem., Int. Ed.*, 2013, **52**, 3621–3625.
35 G. Kresse and J. Furthmuller, *Phys. Rev. B: Condens. Matter Mater. Phys.*, 1996, **54**, 11169.
36 G. Kresse and J. Furthmuller, *Comput. Mater. Sci.*, 1996, **6**, 15–50.
37 P. E. Blochl, *Phys. Rev. B: Condens. Matter Mater. Phys.*, 1994, **50**, 17953.
38 J. P. Perdew, K. Burke and M. Ernzerhof, *Phys. Rev. Lett.*, 1996, **77**, 3865.
39 S. Grimme, *J. Comput. Chem.*, 2004, **25**, 1463–1473.
40 S. Grimme, *J. Comput. Chem.*, 2006, **27**, 1787–1799.
41 W. Geng, X. Zhao, H. Liu and X. Yao, *J. Phys. Chem. C*, 2013, **117**, 10536–10544.
42 W. Hu, Z. Li and J. Yang, *J. Chem. Phys.*, 2013, **138**, 124706.
43 H. J. Monkhorst and J. D. Pack, *Phys. Rev. B: Solid State*, 1976, **13**, 5188.
44 J. P. Perdew, *Int. J. Quantum Chem.*, 1986, **30**, 451–451.
45 J. Heyd, G. E. Scuseria and M. Ernzerhof, *J. Chem. Phys.*, 2003, **118**, 124706.
46 M. Chhowalla, H. S. Shin, G. Eda, L.-J. Li, K. P. Loh and H. Zhang, *Nat. Chem.*, 2013, **5**, 263–275.
47 M. Xu, T. Liang, M. Shi and H. Chen, *Chem. Rev.*, 2013, **113**, 3766–3798.
48 M. Gajdos, K. Hummer, G. Kresse, J. Furthmuller and F. Bechstedt, *Phys. Rev. B: Condens. Matter Mater. Phys.*, 2006, **73**, 045112.
49 C. Ataca, H. Sahin and S. Ciraci, *J. Phys. Chem. C*, 2012, **116**, 8983–8999.
50 C. Ataca, M. Topsakal, E. Akturk and S. Ciraci, *J. Phys. Chem. C*, 2011, **115**, 16354–16361.
51 C. Ataca and S. Ciraci, *Phys. Rev. B: Condens. Matter Mater. Phys.*, 2012, **85**, 195410.
52 Y. Ma, Y. Dai, M. Guo, C. Niu and B. Huang, *Nanoscale*, 2011, **3**, 3883–3887.
53 N. Singh, G. Jabbour and U. Schwingenschlogl, *Eur. Phys. J. B*, 2012, **85**, DOI: 10.1140/epjb/e2012-30449-7.
54 L. Sun, X. Zhao, C.-J. Jia, Y. Zhou, X. Cheng, P. Li, L. Liu and W. Fan, *J. Mater. Chem.*, 2012, **22**, 23428–23438.
55 A. Du, S. Sanvito and S. C. Smith, *Phys. Rev. Lett.*, 2012, **108**, 197207.
56 A. Du, S. Sanvito, Z. Li, D. Wang, Y. Jiao, T. Liao, Q. Sun, Y. H. Ng, Z. Zhu, R. Amal and S. C. Smith, *J. Am. Chem. Soc.*, 2012, **134**, 4393–4397.
57 Z. Alferov, *Semiconductors*, 1998, **32**, 1.
58 J. Tersoff, *Phys. Rev. B: Condens. Matter Mater. Phys.*, 1984, **30**, 4874.
59 Y. Zhu, Y. Dai, K. Lai, Z. Li and B. Huang, *J. Phys. Chem. C*, 2013, **117**, 5593–5598.
60 F. Wu, Y. Liu, G. Yu, D. Shen, Y. Wang and E. Kan, *J. Phys. Chem. Lett.*, 2012, **3**, 3330–3334.
61 T. Ohta, A. Bostwick, T. Seyller, K. Horn and E. Rotenberg, *Science*, 2006, **313**, 951–954.
62 E. Kan, H. Ren, F. Wu, Z. Li, R. Lu, C. Xiao, K. Deng and J. Yang, *J. Phys. Chem. C*, 2012, **116**, 3142–3146.